



Quantum mechanical and quasiclassical Born–Oppenheimer dynamics of the reaction $N_2(X^1\Sigma_g^+) + O(^3P) \rightarrow N(^4S) + NO(X^2\Pi)$ on the N_2O \tilde{a}^3A'' and \tilde{b}^3A' surfaces

Sinan Akpinar^a, Iole Armenise^b, Paolo Defazio^b, Fabrizio Esposito^b, Pablo Gamallo^c, Carlo Petrongolo^{d,e,*}, Ramón Sayós^c

^a Department of Physics, Firat University, 23169 Elazig, Turkey

^b Istituto di Metodologie Inorganiche e dei Plasmi del CNR, Via Amendola 122d, I-70126 Bari, Italy

^c Departament de Química Física i IQTC-UB, Universitat de Barcelona, C/Martí i Franquès 1, 08028 Barcelona, Spain

^d Dipartimento di Chimica, Università di Siena, Via A. Moro 2, I-53100 Siena, Italy

^e Istituto per i Processi Chimico-Fisici del CNR, Via G. Moruzzi 1, I-56100 Pisa, Italy

ARTICLE INFO

Article history:

Available online 18 May 2011

Keywords:

Reaction dynamics
Vibrational effects
Insertion and abstraction mechanisms
WP and QCT snapshots

ABSTRACT

We present the quantum mechanical (QM) and quasiclassical trajectory (QCT) dynamics of the title reaction on two uncoupled surfaces, using a wavepacket (WP) method and considering some $N_2(v,j)$ vibrational and rotational states. The reaction is investigated by calculating initial-state-resolved reaction probabilities, cross sections, and rate constants, which are explained in terms of energy profiles and collision mechanisms. These properties reflect the large endo-thermicity of the reaction and the features of the surfaces. Indeed, at low v values we obtain large thresholds and the lower surface is more reactive than the higher one, whereas at high v the thresholds decrease or disappear and the upper surface becomes more reactive. QM and QCT results are in satisfactory agreement, except some differences at low or high collision energy and temperature. QCT rate coefficients agree also with some published results. WP snapshots and movies of QCT time evolution show clearly abstraction and insertion mechanisms depending on the initial conditions. Insertion proceeds via a reaction complex and we observe a QM Feshbach resonance for a specific initial condition. On the overall, the dynamical observables are consistent with the collision mechanisms.

© 2011 Elsevier B.V. All rights reserved.

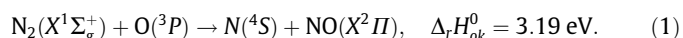
1. Introduction

When a spacecraft enters a planetary atmosphere at speeds exceeding the local speed of sound (hypersonic flow), a shock wave is formed and its kinetic energy is driven into heat. The energy delivered to the gas in this process promotes excitation of the molecular internal degrees of freedom and chemical reactions, including ionization and dissociation. The hot radiating and reacting gas can be in thermal and chemical non-equilibrium, and this molecular plasma interacts later with the vehicle surface, producing heating and surface degradation [1–3].

Advanced entry models mean the description of the non-equilibrium chemical kinetics of the high temperature medium on the basis of a state-to-state approach [4–6], which decomposes any degree of freedom of the molecule in its internal levels. Each level is considered as an independent species, described by an appropriate continuity equation and by its own cross sections and rate coefficients. The thermal properties of the gas and the

global rate coefficients can be calculated from the level distributions and they can deviate from those obtained by assuming a thermal equilibrium or weak non-equilibrium.

At altitudes larger than 60 km for reentry into Earth's atmosphere, spacecrafts have velocities larger than 5 km/s and both N_2 and O_2 can directly dissociate producing $N(^4S)$ and $O(^3P)$ atoms. At much lower altitudes and spacecraft velocities only O_2 can dissociate. Complete sets of state-to-state vibrational-translational and dissociation rate coefficients involving nitrogen and oxygen atoms and molecules can be found in Refs. [7,8]. One of the main bimolecular reactive processes in these hypersonic flows is



In addition, the high interaction energies can also provide relatively efficient vibrational and rotational activation of $N_2(X^1\Sigma_g^+)$ by collision with $O(^3P)$. Reaction (1) is also important in low Earth orbits, where O is the dominant atmospheric species that can react with plume exhaust species, e.g. N_2 arising from N_2O_4 thrusters, or with local environment species, i.e. with N_2 .

Although these elementary processes have important practical implications as above mentioned, only a few experiments have been carried out. Thus, there are some measurements [9,10] of the NO

* Corresponding author at: Dipartimento di Chimica, Università di Siena, Via A. Moro 2, I-53100 Siena, Italy. Fax: +39 0577 234254.

E-mail address: petrongolo@unisi.it (C. Petrongolo).

infrared emissions arising from reaction (1) with hyperthermal O atoms. These experiments show that NO is created rotationally and vibrationally hot and that the reactive cross sections increase with the relative collision energy within the 3.4–7.6 eV range. Moreover, thermal rate constants for a broad set of temperatures are also available [11–13], with a recommended value of $k(T) = 3.0 \times 10^{-10} \exp(-38,300/T) \text{ cm}^3 \text{ s}^{-1}$ over the 1400–4000 K range [14].

From a theoretical point of view, there are scarce studies for reaction (1) although there are many more studies for its reverse reaction $\text{N}({}^4\text{S}) + \text{NO}({}^2\Pi) \rightarrow \text{N}'({}^4\text{S}) + \text{NO}'({}^2\Pi)$ where reactants and products of both reactions correlate through the same two potential energy surfaces (PESs), the first- and second-excited $\tilde{a}^3\text{A}''$ and $\tilde{b}^3\text{A}'$. Early PESs were obtained by using only a few set of *ab initio* data [15–18] and were mainly used for quasiclassical trajectory (QCT) and quantum-mechanical (QM) studies of the N + NO [16,17,19–22] and $\text{N}_2 + \text{O}$ reactions [18,23]. These latter studies presented thermal rate constants $k(T)$ and $k(T_{\text{vib}}, T_{\text{rot}}, T_{\text{trans}})$, and state-specific rates $k_{v,j}(T_{\text{trans}})$ from 3000 to 20,000 K, which is a wide temperature range used in computational fluid dynamics simulations of non-equilibrium flows.

The most recent $\tilde{a}^3\text{A}''$ and $\tilde{b}^3\text{A}'$ analytical PESs [24] were developed by using extensive and much more accurate *ab initio* data [25], and were mainly used for QCT [26] and quantum [27–29] dynamical studies of the N + NO reaction. Furthermore, variational transition state calculations were also performed for reaction (1) using both PESs [24], obtaining an excellent agreement with experimental data [14] at 600–5000 K. It was also demonstrated the importance of the $\tilde{b}^3\text{A}'$ PES at high temperatures: for example, $k(\tilde{a}^3\text{A}'')/k(\tilde{b}^3\text{A}') = 2.9$ at 5000 K.

In this work we present the first QM and QCT dynamics study of reaction (1) using the latest $\tilde{a}^3\text{A}''$ and $\tilde{b}^3\text{A}'$ PESs [24], analyzing the effects of the reactant energy modes on the initial-state-resolved collision observables. This paper is organized as follows: the main characteristics of PESs are briefly described in Section 2, some details regarding the dynamical methods are presented in Section 3, initial-state-resolved reaction probabilities, cross sections, and rate constants are reported in Section 4, we discuss the collision mechanisms in Sections 5 and 6 contains the main concluding remarks.

2. Potential energy surfaces

The PESs used in this work were derived from *ab initio* electronic structure calculations [25] by means of second-order perturbation theory on a complete active-space self-consistent-field wave function (CASPT2 method) in which the standard correlation-consistent polarized valence triple zeta basis set of Dunning [30] was used. The dynamic correlation was treated using the CAS-PT2 method with the G2 correction to the Fock matrix [31].

Stationary points and a broad set of *ab initio* points (5600 and 4900 points for $\tilde{a}^3\text{A}''$ and $\tilde{b}^3\text{A}'$, respectively) were fitted along with some diatomic spectroscopic data to better account for the experimental endo-thermicity.

An energy description of all the processes that can occur in this system is showed in Fig. 1, where we plot some diatomic vibrational and rotational levels $E_{v,j}$ and zero-point energies (ZPEs) of the stationary points of both PESs. In particular, four $\text{N}_2(X^1\Sigma_g^+, v, j)$ vibrational levels at $j = 0$ are drawn: the ground one ($v = 0$), the lowest level above the $\text{N} + \text{NO}$ product energy ($v = 13$), and those at $v = 5$ and $v = 20$ whose cross sections are calculated in this work. The $\text{NO}({}^2\Pi, v = 0, j' = 1)$ ground-state energy is also marked out, noting that $j' \geq 1$.

In the N-abstraction channel, the energy barrier corresponds to the whole endo-thermicity in the case of the $\tilde{a}^3\text{A}''$ PES, while in the case of the $\tilde{b}^3\text{A}'$ PES an extra contribution to the barrier comes from the transition state TS1. Another important feature of the PESs is that they describe also the N-exchange reaction (e), $\text{N}({}^4\text{S}) + \text{N}'\text{O}({}^2\Pi) \rightarrow \text{N}'({}^4\text{S}) + \text{NO}({}^2\Pi)$ whose minimum energy path has a similar shape in both PESs: a C_{2v} minimum (MIN1) connected to two C_s transition states (TS2 and TS2') with exchanged N–O and N'–O bond lengths. This channel was not described in the previous analytical PESs [16–18]. The existence of MIN1 allows a new pathway for reaction (1), via an O-insertion mechanism. Therefore, two possible mechanisms will be possible for reaction (1): a direct N-abstraction or an indirect O-insertion via MIN1, at low or high energies, respectively. This latter mechanism should produce long-lived complexes associated with the profile TS2-MIN1-TS2'. Once the complex is formed the system can evolve towards products $\text{N} + \text{N}'\text{O}$ or $\text{N}' + \text{NO}$ (indistinguishable channels) or dissociate back to reactants ($\text{N}_2 + \text{O}$).

The high accuracy of the present PESs is evidenced by the good agreement with the experimental data, reported in all the previous calculations for both reaction (1) and its reverse, as it was mentioned in the previous section.

3. Methodology

3.1. QM calculations

We obtain initial-state-resolved reaction probabilities $P_{eijk}^{lp}(E_{\text{col}})$ via a time-dependent formalism, propagating wavepackets (WPs) in reactant Jacobi coordinates R , r , and γ , and afterwards performing a flux analysis [32,33]. Here J and p label the total angular momentum and parity quantum numbers, respectively, $e = a$ or b shows the $\tilde{a}^3\text{A}''$ or $\tilde{b}^3\text{A}'$ N_2O electronic states, respectively, v and j are N_2 vibrational and rotational states, respectively, $K \leq \min(J, j)$ is the initial projection of both J and j on \mathbf{R} , and E_{col} is the collision energy. Owing to the involved heavy atoms and the large basis

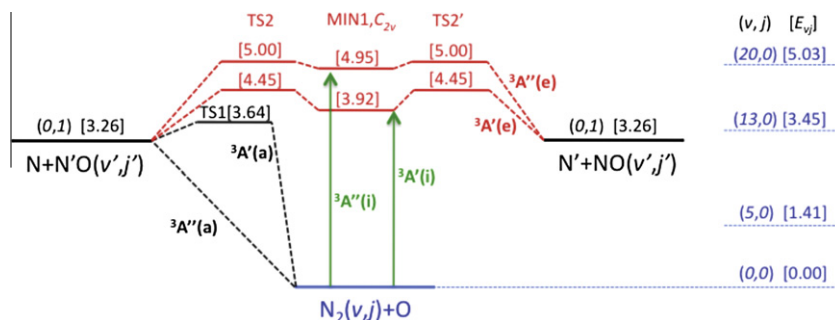


Fig. 1. Energy diagram of $\text{N}_2(v,j) + \text{O}$ reaction. Blue lines are used for describe vibrational–rotational levels (v, j) of the N_2 molecule. Black lines show the N-abstraction mechanism through the $\tilde{a}^3\text{A}''$ and $\tilde{b}^3\text{A}'$ PESs. The red lines are related with the N-exchange mechanism. Finally, the green lines indicate the O-insertion mechanism. Energies in eV, including the ZPEs of the stationary points.

Table 1

Parameters of the QM calculations. Values in atomic units, unless otherwise specified.

Sinc initial WP				
Translational energy center	1.1 eV			
R center and width α	10 and 36			
Smoothing parameter β	0.1			
R range and number of grid points	0–14.5	359		
r range and number of grid points	1.5–14.5	279		
Number of associated Legendre functions and of γ points		80		
R and r absorption start at	11.5			
Absorption strength	0.01			
Flux analysis at r	11			

dimensions that are necessary for converging probabilities at high v, j , and E_{col} , we employ the centrifugal sudden (CS) approximation at some J values and we subsequently interpolate other J probabilities as in Ref. [34]. For both PESs, CS calculations are performed at $J = K, 40, 80, 120$, and 160 for $v = 5$, and at $J = K, 70, 140, 210$, and 280 for $v = 20$, with $j = 0$ and 20 , and $E_{\text{col}} \leq 4$ eV. We have also investigated $\text{N}_2(v, j)$ vibrational and rotational effects on both PESs by computing reaction probabilities at many other v and j values. Initial WPs are defined and propagated via the numerical parameters of Table 1, i.e. using 8,012,880 basis functions.

3.2. QCT calculations

Quasiclassical calculations have been performed in a distributed environment [35] using a numerical code entirely developed by some of us. This code, used many times on different systems [36–38], is optimized for very intensive calculations, which normally include the entire set of rovibrational states supported by the PES asymptotes as initial/final states of trajectory computations. Particular attention has been devoted to the use of an integration checking procedure in order to tune accurately the time step to the features of the dynamics step by step, with a large gain (typically one order of magnitude) in computational resources with respect to a fixed time step procedure for a similar level of accuracy [39]. Collision energy in the center of mass system is uniformly distributed in the range between 1 meV and 10 eV. Stratified sampling is applied. A uniform density of trajectories has been imposed, with 40,000 trajectories per eV of collisional energy and per Å of impact parameter b , which accounts for a total of not less than 13 millions trajectories for the four initial states here presented.

3.3. Cross sections and rate constants

Initial-state-resolved cross sections $\sigma_{evj}(E_{\text{col}})$ and rate constants $k_{evj}(T = T_{\text{trans}})$ have been obtained with the usual expressions, computing QM and QCT cross sections up to $E_{\text{col}} = 4$ and 10 eV, respectively, and rate constants from 300 to 10,000 K.

Finally, we have averaged these observables over the initial unresolved states taking into account both electronic and nuclear-spin degeneracies. The nuclear-spin statistics of $\text{N}_2(X^1\Sigma_g^+) + O(^3P)$ is similar to that of $C(^1D) + D_2(X^1\Sigma_g^+)$ shown in Table 1 of Ref. [40], because both ^{14}N and D are bosons with nuclear spin equal to 1. Therefore, the overall molecular states, including nuclear-spin states, must be symmetric under the permutation of the ^{14}N nuclei. Using the permutation-inversion group $C_{2v}(M)$, Table 2 reports the symmetries of the electronic states $|e\rangle$, the parities of the rotational quantum numbers j , the symmetries of the WPs $|\psi_{evjK}^{lp}\rangle$ and of the associated nuclear-spin states $|I\rangle$, and the nuclear-spin statistical weights w_{ej} . The degeneracy-averaged cross sections σ_{vj} and rate constants k_{vj} are thus equal to

$$\sigma_{vj} = \frac{1}{3} \left(\frac{2}{3} \sigma_{avj} + \frac{1}{3} \sigma_{buj} \right), \quad k_{vj} = \frac{1}{3} \left(\frac{2}{3} k_{avj} + \frac{1}{3} k_{buj} \right), \quad j = \text{even}, \quad (2.1)$$

Table 2

Collision $^{14}\text{N}_2(^1\Sigma_g^+, j) + O(^3P) \rightarrow ^{14}\text{N}_2\text{O}(e)$. Symmetries of molecular-states and nuclear-spin weights.

$ e\rangle$	j	$ \psi_{evjK}^{lp}\rangle$	$ I\rangle$	w_{ej}
\tilde{a}^3A_2	Even	A_1 or A_2	${}^5+1A_1$	2/3
	Odd	B_1 or B_2	3B_2	1/3
\tilde{b}^3B_2	Even	B_1 or B_2	3B_2	1/3
	Odd	A_1 or A_2	${}^5+1A_1$	2/3

$$\sigma_{vj} = \frac{1}{3} \left(\frac{1}{3} \sigma_{avj} + \frac{2}{3} \sigma_{buj} \right), \quad k_{vj} = \frac{1}{3} \left(\frac{1}{3} k_{avj} + \frac{2}{3} k_{buj} \right), \quad j = \text{odd}, \quad (2.2)$$

where the common factor 1/3 takes into account the reactant electronic degeneracy whereas 2/3 and 1/3 are the nuclear-spin weights.

4. Reaction probabilities, cross sections, and rate constants

4.1. Reaction probabilities

$\text{N}_2(v, j)$ vibrational and rotational effects are shown in Fig. 2 that reports $J = 0$ reaction probabilities $P_{evj}^0(E_{\text{col}})$ on both PESs, for several v and j values. It is worth noting that $v = 13$ or 14 are the first $\text{N}_2(v, 0)$ vibrational levels with energy larger than the \tilde{a}^3A'' endo-thermicity or the \tilde{b}^3A' TS1 barrier, respectively. For brevity sake, we do not show probabilities at $J > 0$, which are available to the interested reader and show the usual J shifting, roughly proportional to $J(J + 1)$.

Owing to the large endo-thermicity of the reaction (1), the probabilities present large thresholds when N_2 is weakly excited, which decrease mainly with v and slightly with j , and which are larger than the abstraction static ones deduced from Fig. 1. The \tilde{a}^3A'' or \tilde{b}^3A' thresholds thus disappear only at $v \sim 23$ or 20 , respectively, that is at much higher $\text{N}_2 E_{vj}$ energies than those at $v = 13$ or 14 shown in Fig. 1. This implies an insertion collision on both PESs, in addition to the abstraction one, along the TS2-MIN1-TS2' profile of Fig. 1. Note that the $\text{N}_2(20, 0) + \text{O}$ collision on the \tilde{a}^3A'' PES still presents a threshold of ~ 0.3 eV, although $E_{20,0}$ is much greater than the energy of the $\text{N} + \text{NO}(0, 1)$ products and is nearly thermo-neutral with TS2 of this surface.

Moreover, $P_{evj}^0(E_{\text{col}})$ increase or decrease at small or large E_{col} , respectively, reaching maximum values that depend on the initial conditions, and the $v = 20$ probabilities are rather small at $E_{\text{col}} > 1.6$ –1.8 eV. Up to ~ 0.8 eV above the threshold energy, \tilde{a}^3A'' probability resonances are very weak, but they are clearly seen at higher energies or on the \tilde{b}^3A' surface, in agreement with direct (abstraction) or indirect (insertion) collisions, respectively. Comparing probabilities on both PESs, we find that \tilde{a}^3A'' is more reactive than \tilde{b}^3A' up to $v \sim 13$, that is when the reaction is endo-thermic. On the contrary, when N_2 is more vibrationally excited, the \tilde{b}^3A' surface becomes more reactive.

4.2. Cross sections

Fig. 3 presents initial-state selected cross sections $\sigma_{evj}(E_{\text{col}})$, QM up to $E_{\text{col}} = 4$ eV in the left panels and QCT up to $E_{\text{col}} = 10$ eV in the right panels. We show results on both surfaces, at $v = 5$ and $20, j = 0$ and 20 .

According to the probability results, the QM cross sections depend clearly on the endo-thermicity or exo-thermicity of the initial-state-resolved reactions, that is on the N_2 vibrational level. When $v = 5$, in fact, $\sigma_{e,5,j}$ present large thresholds equal to ~ 2.1 – 2.5 eV, depending on e and j , and increase monotonically with E_{col}

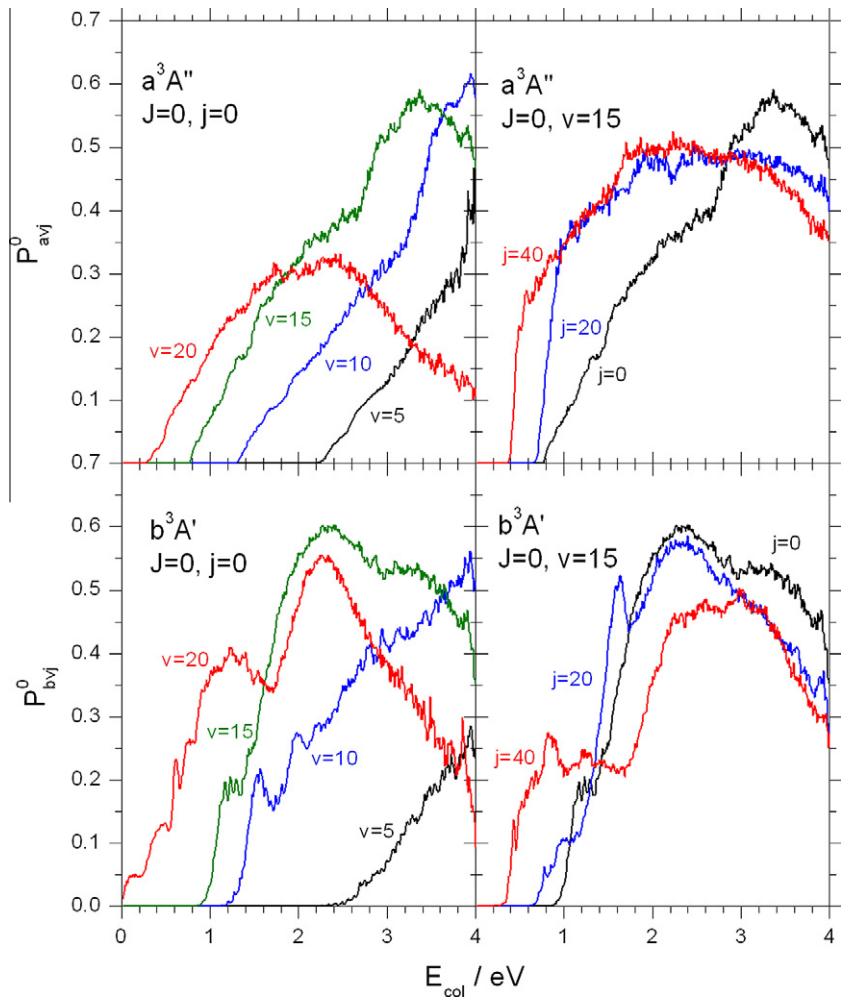


Fig. 2. QM $J = 0$ reaction probabilities $P_{eij}^0(E_{col})$.

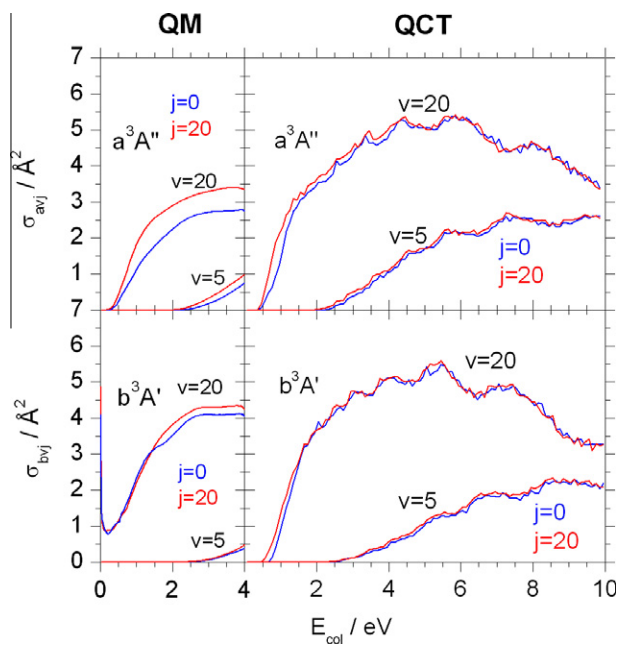


Fig. 3. QM (left panels) and QCT (right panels) initial-state-resolved cross sections $\sigma_{eij}(E_{col})$.

up to $\sigma_{a,5,20}(4\text{eV}) = 0.99 \text{ Å}^2$. The results at $v = 20$ are different for the two PESs: that is, with a threshold of ~ 0.3 eV for \tilde{a}^3A'' or without any threshold for \tilde{b}^3A' , as we found for the corresponding probabilities of Fig. 2. The \tilde{a}^3A'' $\sigma_{a,20,j}$ increase monotonically up to 4 eV, whereas those on the \tilde{b}^3A' surface are large at small collision energies, decrease for $E_{col} < 0.2$ eV, and finally increase at higher energies.

The bimodal behavior of the cross sections on the \tilde{b}^3A' PES for $v = 20$ is rather interesting and is similar to that of O (1D) + H₂ observed by Liu [41]. It can be explained in two ways: the first is based on the results discussed up to now and the second relies on the discussion of Ref. [41] and on the reaction mechanisms that we shall present in Section 5. Fig. 1 shows that the energy of the N₂(20,0) + O reactants is much larger than that of the N + NO(0,1) products, and even higher than that of the \tilde{b}^3A' TS2 by 0.58 eV. At these initial conditions, therefore, the reaction is exo-thermic and barrierless, hence the probability $P_{b,20,j}^0$ of Fig. 2 is threshold-less and small up to ~ 0.2 eV. The $1/E_{col}$ factor of the QM cross section thus gives large and decreasing $\sigma_{b,20,j}$ up to ~ 0.05 eV (Fig. 3). At collision energies larger than ~ 0.2 eV, however, the steep probability rise compensates the decreasing $1/E_{col}$ factor and $\sigma_{b,20,j}$ increase.

Fig. 3 also shows that the N₂ vibrational and rotational excitation favors preferentially the \tilde{b}^3A' reactivity, and that vibrational or rotational effects are more important on the \tilde{b}^3A' or \tilde{a}^3A'' surface, respectively.

The QCT cross sections of Fig. 3 are in general larger than the QM ones, except those on the \tilde{b}^3A' PES at $v = 20$ and small E_{col} . At

this initial condition, indeed, the QM results do not have any threshold, contrary to the QCT onsets at ~ 0.5 eV. This difference is a purely quantum effect associated with the QM $1/E_{\text{col}}$ factor that is absent in the QCT σ . In general, however, QM and QCT cross sections are in acceptable agreement. This is encouraging for the reliability of much more extended QCT studies in which many other possible initial rovibrational states will be considered. This kind of calculation, unfeasible with accurate quantum methods, is currently performed with quasiclassical methods on distributed computational resources [35].

Averaging the initial-state-resolved cross sections as in Eq. (2.1), we obtain the observable cross sections $\sigma_{vj}(E_{\text{col}})$ plotted in Fig. 4. The energy range is limited to 4 eV for a better comparison between QM and QCT results. Of course, these averaged results reflect closely those selected on the initial states and the nuclear-spin statistics of Eq. (2.1). Therefore, the QM σ_{vj} show clearly the importance of the upper \tilde{b}^3A' surface at $v = 20$ and small E_{col} , whereas the QCT σ_{vj} increase faster with the collision energy than the QM ones. At large E_{col} , the lower \tilde{a}^3A'' surface is more important owing to the associated 2/3 nuclear-spin weight of Eq. (2.1).

4.3. Rate constants

The logarithms of the QM and QCT degeneracy-averaged rate constants $k_{vj}(T)$ are reported in Table 3 at $T = 2000$ and 10,000 K, and are plotted in Fig. 5. For comparison, we show in Table 3 some previous QCT results [18]. As expected from the energy diagram of Fig. 1, the reaction occurs at room temperature only for $v = 20$, with QM or QCT rate constants equal to about 10^{-12} or 10^{-18} $\text{cm}^3 \text{s}^{-1}$, respectively. This large difference is due to the different $\sigma_{b,20,j}$ at low E_{col} . In general, large vibrational and temperature effects are found on these rate constants, up to 5.8 orders of magnitude for the QM $k_{v,0}(2000)$ from $v = 5$ to 20, and up to 5.4 orders of magnitude for the QCT $k_{v,0}$ from 2000 to 10,000 K. On the other hand, rotational effects are less important or negligible for $v = 20$. QCT rate constants are in really good agreement with the Bose and Candler [18] values at 10,000 K, as can be seen in Table 3, taking into account that the previous QCT calculations did not consider the nuclear-spin weights of Eq. (2.1).

Finally, Fig. 5 reveals a good global agreement for QM and QCT averaged rate constants from 2000 to 10,000 K, mainly at low temperatures and for the $v = 20$ case.

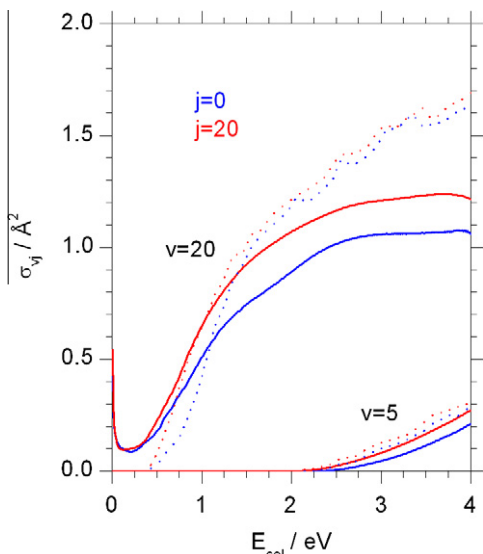


Fig. 4. QM (full) and QCT (dot) degeneracy-averaged cross sections $\sigma_{vj}(E_{\text{col}})$.

Table 3

Logarithms of the degeneracy-averaged rate constants $k_{vj}/\text{cm}^3 \text{s}^{-1}$ at 2000 and 10,000 K.

v	j	Method	2000 K	10,000 K [18] ^a
5	0	QM	-17.5	-12.3
		QCT	-16.6	-11.2(-11.5)
5	20	QM	-12.1	-17.0
		QCT	-16.2	-11.2
20	0	QM	-11.7	-10.6
		QCT	-11.7	-9.95(-10.2)
20	20	QM	-11.5	-10.5
		QCT	-11.4	-9.91

^a Without the nuclear-spin weights of Eq. (2.1).

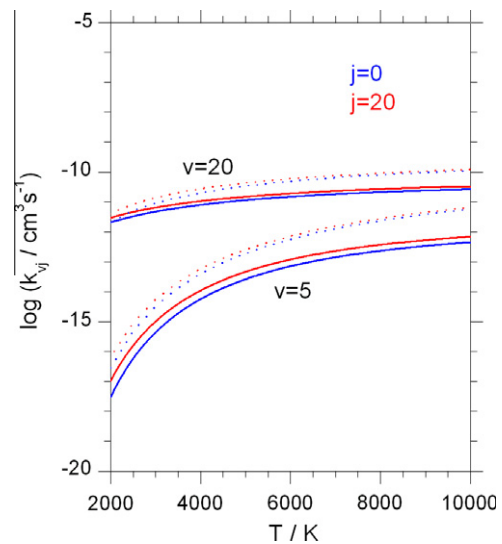


Fig. 5. QM (full) and QCT (dot) logarithms of the degeneracy-averaged rate constants $k_{vj}(T)$.

5. Collision mechanisms

5.1. QM calculations

For a better explanation of the results of the previous section, we discuss QM collision mechanisms by studying WP time-evolutions at different initial conditions. Snapshots of the γ -averaged WP densities show clearly that the $v = 20$ densities in the N + NO product channel are much larger than those at $v = 5$, in agreement with the large vibrational enhancement of the reactivity shown in Figs. 2–5. Detailed mechanisms are, however, better described by snapshots of the r -averaged WP densities,

$$\rho_{ev0}^0(R, \gamma, t) = \langle \psi_{ev0}^0(R, r, \gamma, t) | \psi_{ev0}^0(R, r, \gamma, t) \rangle_r, \quad (3)$$

where $J = 0$, $e = \tilde{a}^3A''$ and \tilde{b}^3A' , $v = 5$ and 20, $j = 0$, and $t = 50$ and 75 fs. These conditions correspond to endo-thermic or exo-thermic collisions and to WPs in the strong interaction regions of the potentials. From [24] and Fig. 1, abstraction occurs mainly at $\gamma < 50^\circ$ or at $\gamma > 130^\circ$ and at low energies, whereas insertion is predominant at $50^\circ < \gamma < 130^\circ$ and at high energies. According to this, Fig. 6 shows the following mechanisms at these initial conditions:

1. $\tilde{a}^3A'', v = 5$. At 50 fs the WP spreads on both quasi-collinear and orthogonal regions of the surface, showing both abstraction (preferred) and insertion mechanisms. At 75 fs, the WP is reflected back by the repulsive wall of the PES, with $4 < R < 6a_0$.
2. $\tilde{a}^3A'', v = 20$. At 50 fs, the WP is delocalized on a wide R and γ region. The WP density is larger at $\gamma \sim 90^\circ$, implying a preferred insertion mechanism, but the large γ variation shows an

orbiting motion of the approaching O atom towards the highly oscillating N_2 diatom. At 75 fs, however, we see only an insertion collision and a strongly trapped WP at $R \sim 3.5 a_0$ and $\gamma = 90^\circ$. This implies the formation of quasi-bound, high-energy states of a N_2O collision complex, and this is a purely dynamical effect due to the high N_2 vibrational energy, because it is absent at $v = 5$. This is the signature of a purely QM Feshbach resonance [42] and of an inelastic energy transfer. For example, the $VR-V'R'$ processes $N_2(20,j) + O \rightarrow N_2(v' < 20,j') + O$ should be quite efficient, because they are favored by the high N_2 excitation, by the high density of states of a very excited N_2O complex, and by the very low MIN1 asymmetric frequency $\omega_3 \approx 42 \text{ cm}^{-1}$ [24] (the normal mode associated with reaction coordinate). These non-reactive collisions decrease the QM reactive probabilities and cross sections, as Figs. 2 and 3 show. In particular, the Feshbach resonance can explain the threshold and the high-energy decrease of $P_{a,20,0}^0$ shown in the upper left panel of Fig. 2. The N_2O complex breaks down after ~ 70 fs, in a non-reactive or reactive way with both abstraction and insertion mechanisms.

3. $\tilde{b}^3A', v = 5$. Abstraction is the predominant mechanism at 50 fs, because the WP mean energy is not enough for overcoming the TS2 barrier.

4. $\tilde{b}^3A', v = 20$. At 75 fs we find both abstraction and insertion mechanisms and a less localized WP with respect to the \tilde{a}^3A'' one. The intramolecular energy transfer is now less efficient than for \tilde{a}^3A'' , probably owing to the smaller density of states of the \tilde{b}^3A' MIN1 with $\omega_3 = 1234 \text{ cm}^{-1}$ [24]. This implies shorter-lived N_2O complexes and a larger \tilde{b}^3A' reactivity at $v = 20$, as we actually find. The presence of both abstraction and insertion mechanisms can give the second explanation of the peculiar shape of the \tilde{b}^3A' cross sections for $v = 20$, following the interpretation of Ref. [41].

5.2. QCT calculations

Collision mechanisms can be also studied in detail by using quasiclassical trajectories. With the aim of reproducing as close as possible the WP snapshots, we propose here a graphical representation of the QCT dynamics that we call “trajectory fireworks”. It consists of representing a relatively small bunch of trajectories as a function of R and γ Jacobi coordinates, ignoring the value of the N_2 internuclear distance r . Adopting a fixed integration time step of 0.01 fs for the calculation of all the trajectories of the bunch, the whole time evolution is represented by using frames at a fixed time interval of 1 fs, in order to show what would occur if all the

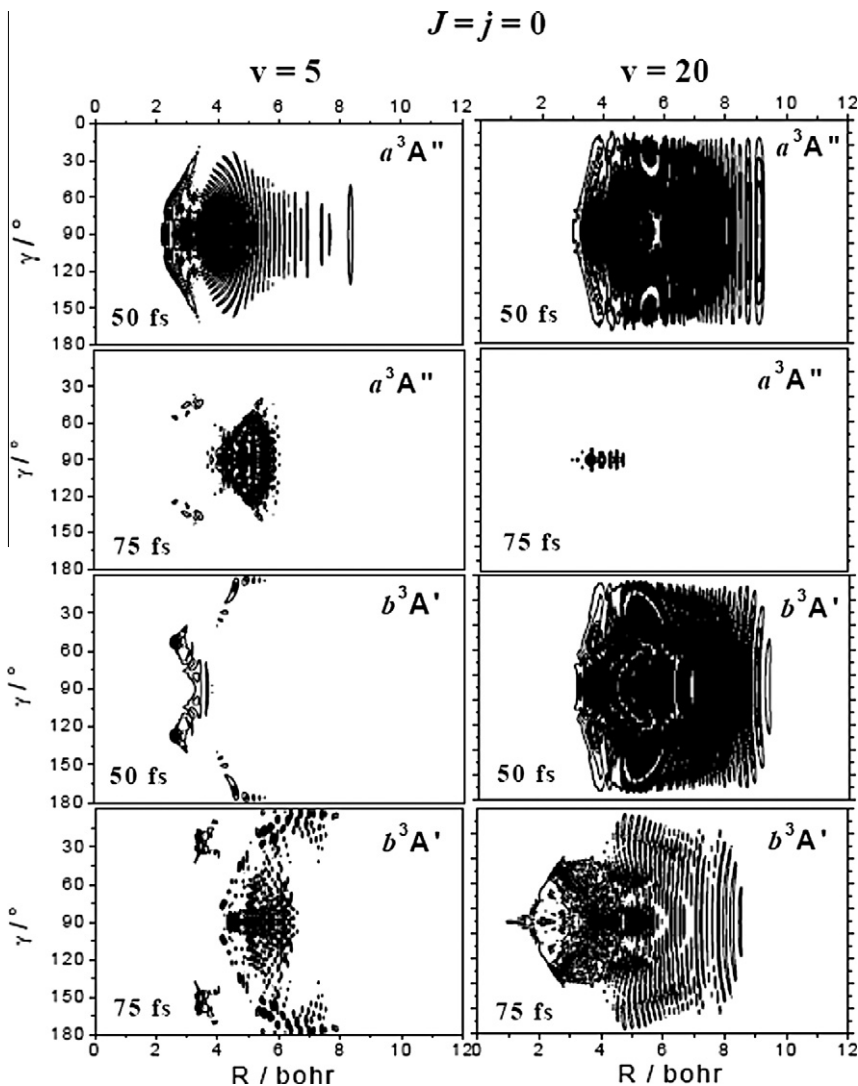


Fig. 6. WP snapshots at $J = 0$, $e = \tilde{a}^3A''$ and \tilde{b}^3A' , $v = 5$ and 20, $j = 0$, and $t = 50$ and 75 fs. See Eq. (3).

trajectories were integrated simultaneously. Of course, no interaction exists among different trajectories, in contrast to what happens among various parts of a propagating WP: this is a fundamental difference between classical and quantum propagations [43]. The bunch of trajectories has a uniform velocity distribution between 0.1 and 4 eV that is approximately the energy interval where there is significant probability density of the corresponding wave packet. Trajectories start at $R = 10 a_0$ in the first frame of the sequence. Every fs a new representative frame is generated, displaying for each trajectory the position at that time as a point (the “head”), and the three positions at the preceding 3 fs as a line (the “tail”). We call “comet” the set of head and tail of a given trajectory. The density of heads gives an idea of the probability density in different regions, while the tails allow following the short time evolution of each trajectory. We assign a color to each comet on the base of the following criterion. If $R > r$ the comet is red, meaning either the trajectory is yet approaching the strong coupling region or it is receding from it in a non-reactive way. If $R < 4r/7$, the color is blue: in this case for low R values the system is in the strong coupling region, while for R larger than $\sim 4 a_0$ the trajectory is probably reactive and is essentially at the end of its evolution. The intermediate condition $4r/7 < R < r$ is represented by the green color. Of course, the distinction between reactive and non-reactive comets is approximated because it is considered during the time evolution. It is, however, statistically correct because QCT results show that the character of each trajectory is essentially conserved in time after the first strong interaction. Trajectory snapshots at selected times are plotted in Figs. 7 and 8 and full movies between 10 and 150 fs are available in the electronic version of this paper, showing much more details. For facilitating the comparison with QM results, the total angular momentum J is fixed to zero by treating all the cases for $j = 0$ and fixing to zero the impact parameter. According to this, Figs. 7 and 8 are analyzed below.

1. \tilde{a}^3A'' , $v = 5$. In Fig. 7a a particular frame at $t = 80$ fs is displayed. There, it is possible to distinguish on the right very slow trajectories (represented by small tails) that at that time have yet to reach the strong coupling region. For $5 \leq R \leq 7a_0$, it is possible to see moderately faster trajectories going towards lower R values with a nearly constant γ angle, but also some very fast trajectories that have been “backscattered” by the PES wall with a wide distribution of tail slopes, giving a sort of “explosion”. This is mainly attributed to the fact that all trajectories have been calculated at $b = 0$ and this approach is highly repulsive at the $v = 5$ energy. This red explosion is quite evident in all the cases, describes non-reactive collisions, and is in nice agreement with the WP plot of Fig. 6 on \tilde{a}^3A'' , at $v = 5$ and $t = 75$ fs. In the region between $R = 2$ and $3.5 a_0$, two very clear green-blue regions are present, symmetrical disposed around $\gamma \sim 90^\circ$ with $30^\circ \leq \gamma \leq 60^\circ$ on one side and $120^\circ \leq \gamma \leq 150^\circ$ on the other side. It is possible to see also the blue comets curving back in symmetrical ways. This can be attributed easily to a direct mechanism of abstraction, and from the observation of the full movie 1 (online version only) one can also deduce that in this case only this mechanism is relevant. It is interesting the similarity of this distribution with the corresponding quantum one.

2. \tilde{a}^3A'' , $v = 20$. Very different is the case $v = 20$ on the same \tilde{a}^3A'' PES, shown with a snapshot at 80 fs in Fig. 7b, with a high density region around $R = 3 a_0$ and $\gamma \sim 90^\circ$. Also in this case there is a similarity with the QM evolution at 75 fs without, of course, the presence of the quantum resonance, and this is true also at later times, when two symmetrical regions away from $\gamma = 90^\circ$ are present in both QM and QCT representations. From careful inspection of the Fig. 7b, and more easily in the related movie 2 (online version only), one can deduce that the insertion

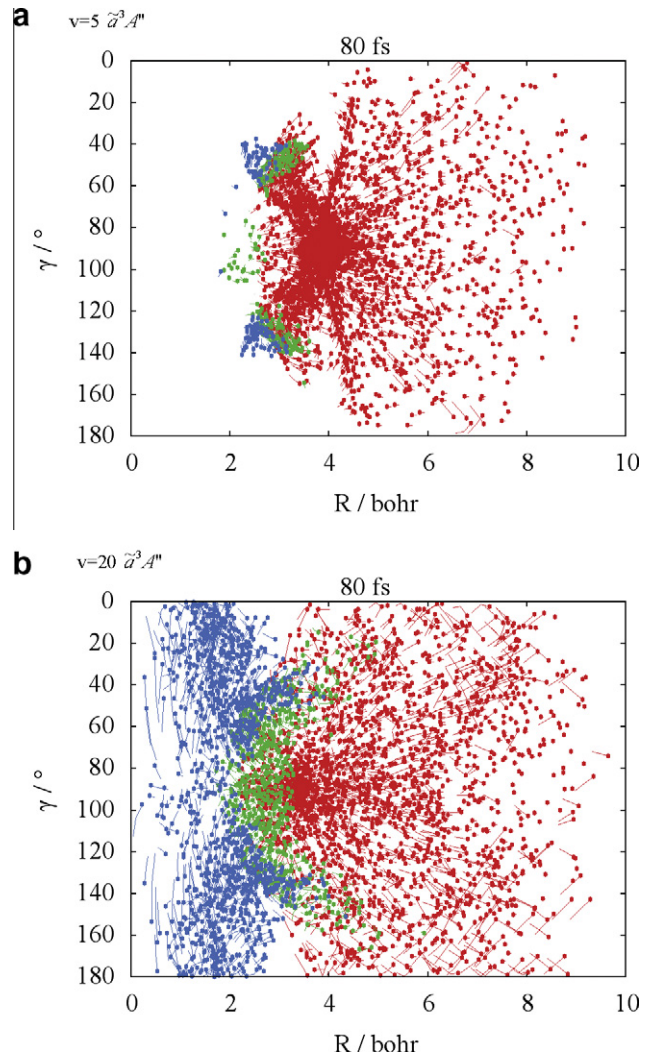


Fig. 7. \tilde{a}^3A'' QCT snapshots at $v = 5$ and 20. See text for details.

mechanism, with complex formation, is surely predominant in this case. The complexes are visible as very complicated and whirled blue comets at 50 and 55 fs in the movie 2. Later, these insertion comets describe a large loop changing significantly their γ angle towards one of the two extrema. This corresponds quite reasonably to traversing the TS2 or TS2' transition state of Fig. 1. For times later than 65 fs, a certain amount of green and blue, strongly interacting trajectories are located at angles away from 90° and between $R = 3$ and $5 a_0$. By following their evolution between 65 and 80 fs, one can easily see that they are generated in that region; therefore they appear related to an abstraction mechanism rather than an insertion one. At $t > 100$ fs, these abstraction trajectories merge with the other insertion blue comets. It is also important to stress that merging all the colored densities into one would bring to quite different conclusions, because of the presence of a large density of predominantly non-reactive trajectories.

3. \tilde{b}^3A' , $v = 5$. In Fig. 8a at $t = 80$ fs it is very clear a sort of narrow channel around $\gamma \sim 90^\circ$ for $R < 2 a_0$. By inspecting the movie 3 (online version only) it is possible to see clearly that it is originated from a bunch of complexes in a green quite small area for $t > 50$ fs, while the very fast spanning of angle domain for $R < 0.5 a_0$ is the already explained insertion mechanism of transition state traversing after reached the MIN1 minimum in Fig. 1. Few abstraction green trajectories are seen at low and

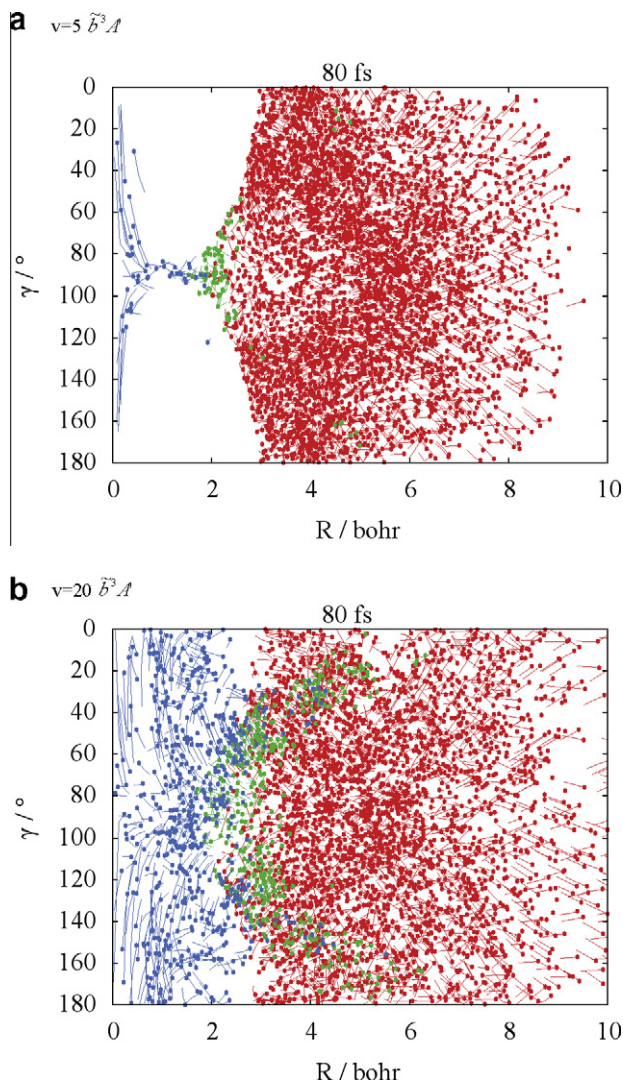


Fig. 8. \tilde{b}^3A' QCT snapshots at $v = 5$ and 20. See text for details.

high angles between 4 and 5 bohr, clearly not related to insertion complexes. If the impact parameter is increased, the abstraction mechanism is obviously favored.

4. $\tilde{b}^3A', v = 20$. In Fig. 8b and in the related movie 4 (online version only), the case $v = 20$ on the upper surface is qualitatively similar to what is obtained in the same condition on the lower PES, but with a more relevant presence of the abstraction mechanism, associated with green small and large angle regions at $R > 3a_0$.

Summarizing the QCT results, on the lower \tilde{a}^3A'' PES at $v = 5$ the abstraction mechanism is clearly predominant, at $v = 20$ the insertion mechanism with short-lived complex formation is the preferred one, with a small contribution from abstraction. On the upper \tilde{b}^3A' PES, at $v = 5$ the insertion mechanism is predominant, because the TS2 barrier of this surface is lower than that of \tilde{a}^3A'' (Fig. 1), while at $v = 20$ both mechanisms are important. Therefore, QM and QCT collision mechanisms and time evolutions agree in the main features of the mechanisms, the main differences being the QM resonance on \tilde{a}^3A'' at $v = 20$ and the different mechanisms on \tilde{b}^3A' at $v = 5$.

6. Conclusions

We presented the QM and QCT dynamics of the reaction $N_2(X^1\Sigma_g^+, v, j) + O(^3P) \rightarrow N(^4S) + NO(X^2\Pi)$ on the uncoupled N_2O

\tilde{a}^3A'' and \tilde{b}^3A' PESs. We propagate real CS WP, obtaining QM reaction probabilities via a flux analysis, and we run large bunches of quasiclassical trajectories. We calculate initial-state-resolved probabilities, cross sections, and rate constants, taking into account the Pauli principle for the ^{14}N bosons and contrasting the results of both methods. We also investigate the collision mechanisms via QM-WP and QCT snapshots in real time.

Because the reaction is strongly endo-thermic, high v values or collision energies are necessary for obtaining an appreciable formation of the products. Therefore, reaction probabilities and cross sections present large thresholds at low v values, which are strongly reduced or disappear by increasing v . However, the N_2 vibrational energy is rather inefficient in promoting the reaction and the collision energy is hardly transformed in the potential one for overcoming the reaction barriers, as expected for a late barrier situation. The reaction probabilities point also out direct or indirect processes at low or high energy, respectively. The lower \tilde{a}^3A'' PES is more reactive than the \tilde{b}^3A' one up to $v = 13$, whereas the upper surface becomes more reactive at higher v values as clearly seen at $v = 20$. We find a satisfactory agreement between QM and QCT results, despite some differences at very small or rather large E_{col} values. The N_2 vibrational excitation and the temperature enhance the rate constants up to 5.8 orders of magnitude. Finally, QM and QCT rates compare rather well and the latter are also in good agreement with some earlier computational results.

The analysis of the WP and QCT time-evolutions shows two possible collision mechanisms, abstraction at low energies and insertion at high energies, depending on the initial condition and time. On the upper \tilde{b}^3A' PES the insertion mechanism is predominant at $v = 5$, while both insertion and abstraction are important at $v = 20$. On the lower \tilde{a}^3A'' PES, abstraction mechanism occurs mainly at $v = 5$ contrary to the predominant insertion mechanism observed at $v = 20$, which produces high-energy N_2O complexes. In the latter case, the WP time evolution suggests the formation of a quasi-bound Feshbach resonance, associated with an inelastic collision that reduces the N_2 vibrational energy. This mechanism is absent on both PESs when N_2 is moderately vibrationally excited, or is significantly quenched on the upper surface even at high v quanta. Of course, this is purely QM effect that cannot be observed in QCT calculations. However, QM and QCT mechanisms are in good agreement at other initial conditions.

Acknowledgements

This work was supported by the ESA-ESTEC of Noordwijk, The Netherlands, under contract 21790/08/NL/HE, by the European Community under the FP7 Research Infrastructures Programme, by the HPC-EUROPA2 project 228398, by the Spanish Ministry of Science and Innovation, project CTQ2009-07647, and by the Autonomous Government of Catalonia, project 2009SGR1041. The research leading to these results has received funding from the European Community's Seventh Framework Programme (FP7/2007–2013) under grant agreement n° 242311. We also thank the CINECA supercomputer center of Bologna, Italy, the University of Siena, and the IPCF-CNR of Pisa.

Appendix A. Supplementary data

Supplementary data associated with this article can be found, in the online version, at doi:10.1016/j.chemphys.2011.05.005.

References

- [1] J.J. Bertin, R.M. Cummings, Annu. Rev. Fluid Mech. 38 (2006) 129.
- [2] I. Armenise, M. Capitelli, S. Longo, J. Thermophys. Heat Trans. 23 (2009) 674.

- [3] I. Armenise, M. Barbato, M. Capitelli, E.V. Kustova, *J. Thermophys. Heat Trans.* 20 (2006) 465.
- [4] M. Capitelli, R. Celiberto, F. Esposito, A. Laricchiuta, *Plasma Process. Polym.* 6 (2009) 279.
- [5] I. Armenise, M. Capitelli, *Plasma Sources Sci. Trans.* 14 (2005) S9.
- [6] M. Capitelli, I. Armenise, D. Bruno, M. Cacciatore, R. Celiberto, G. Colonna, O. De Pascale, P. Diomede, F. Esposito, C. Gorse, K. Hassouni, A. Laricchiuta, S. Longo, D. Pagano, D. Pietanza, M. Rutigliano, *Plasma Sources Sci. Technol.* 16 (2007) S30.
- [7] F. Esposito, I. Armenise, M. Capitelli, *Chem. Phys.* 331 (2006) 1.
- [8] F. Esposito, I. Armenise, G. Capitta, M. Capitelli, *Chem. Phys.* 351 (2008) 91.
- [9] B.L. Upsilonchulte, D.B. Oakes, G.E. Caledonia, W.A.M. Blumberg, *Geophys. Res. Lett.* 19 (1992) 993.
- [10] D.B. Oakes, D.M. Sonnenfroh, G.E. Caledonia, W.A.M. Blumberg, *J. Geophys. Res.* 99 (1994) 23249.
- [11] H.S. Glick, J.J. Klein, W. Squire, *J. Chem. Phys.* 27 (1957) 850.
- [12] K.L. Wray, J.D. Teare, *J. Chem. Phys.* 36 (1962) 2582.
- [13] R.E. Duff, N. Davidson, *J. Chem. Phys.* 31 (1959) 1018.
- [14] D.L. Baulch, C.J. Cobos, R.A. Cox, P. Frank, G. Hayman, Th. Just, J.A. Kerr, T. Murrells, M.J. Pilling, J. Troe, R.W. Walker, J. Warnatz, *J. Phys. Chem. Ref. Data* 23 (1994) 847.
- [15] S.P. Walsh, R.L. Jaffe, *J. Chem. Phys.* 86 (1987) 6946.
- [16] M. Gilibert, A. Aguilar, M. González, F. Mota, R. Sayós, *J. Chem. Phys.* 97 (1992) 5542.
- [17] J.W. Duff, R.D. Sharma, *Geophys. Res. Lett.* 23 (1996) 2777.
- [18] D. Bose, G.V. Candler, *J. Chem. Phys.* 104 (1996) 2825.
- [19] M. Gilibert, A. Aguilar, M. González, R. Sayós, *J. Chem. Phys.* 99 (1993) 1719.
- [20] R. Sayós, A. Aguilar, M. Gilibert, M. González, *J. Chem. Soc. Farad. Trans.* 89 (1993) 3223.
- [21] J.W. Duff, R.D. Sharma, *Chem. Phys. Lett.* 265 (1997) 404.
- [22] A. Aguilar, M. Gilibert, X. Giménez, M. González, R. Sayós, *J. Chem. Phys.* 103 (1995) 4496.
- [23] D. Bose, G.V. Candler, *J. Therm. Heat Trans.* 10 (1996) 148.
- [24] P. Gamallo, M. González, R. Sayós, *J. Chem. Phys.* 119 (2003) 2545.
- [25] P. Gamallo, M. González, R. Sayós, *J. Chem. Phys.* 118 (2003) 10602.
- [26] P. Gamallo, R. Martínez, R. Sayós, M. González, *J. Chem. Phys.* 132 (2010) 144304.
- [27] P. Gamallo, M. González, R. Sayós, C. Petrongolo, *J. Chem. Phys.* 119 (2003) 7156.
- [28] P. Gamallo, R. Sayós, M. González, C. Petrongolo, P. Defazio, *J. Chem. Phys.* 124 (2006) 174303.
- [29] M. Jorfi, P. Honvau, *J. Phys. Chem. A* 113 (2009) 10648.
- [30] T.H. Dunning, *J. Chem. Phys.* 90 (1989) 1007.
- [31] K. Anderson, *Theor. Chim. Acta* 91 (1995) 31.
- [32] S.K. Gray, G.G. Balint-Kurti, *J. Chem. Phys.* 108 (1998) 950.
- [33] A.J.H.M. Meijer, E.M. Goldfield, S.K. Gray, G.G. Balint-Kurti, *Chem. Phys. Lett.* 293 (1998) 270.
- [34] P. Gamallo, P. Defazio, M. González, C. Petrongolo, *J. Chem. Phys.* 129 (2008) 244307.
- [35] <<http://compchem.unipg.it/>>.
- [36] F. Esposito, M. Capitelli, *J. Phys. Chem. A* 113 (2009) 15307.
- [37] F. Esposito, M. Capitelli, *Chem. Phys. Lett.* 418 (2006) 581.
- [38] F. Esposito, M. Capitelli, *Chem. Phys. Lett.* 443 (2007) 222.
- [39] F. Esposito, M. Capitelli, *Chem. Phys. Lett.* 364 (2002) 180.
- [40] P. Defazio, P. Gamallo, M. González, S. Akpinar, B. Bussery-Honvau, P. Honvau, C. Petrongolo, *J. Chem. Phys.* 132 (2010) 104306.
- [41] K. Liu, *Int. Rev. Phys. Chem.* 20 (2001) 189.
- [42] J.Z.H. Zhang, *Theory and Application of Quantum Molecular Dynamics*, World Scientific, Singapore, 1999.
- [43] F. Esposito, *Lecture Notes Comput. Sci. Part II* 3044 (2004) 300.